

Novel design of a coreless axial-flux permanent-magnet generator with 3-layer winding coil for small wind turbines

ISSN 1752-1416
 Received on 2nd August 2019
 Revised 21st July 2020
 Accepted on 26th August 2020
 E-First on 12th November 2020
 doi: 10.1049/iet-rpg.2019.0908
 www.ietdl.org

Wu-Sung Yao, Ming-Te Cheng, Jyh-Cheng Yu*

Department of Mechatronics Engineering, National Kaohsiung University of Science and Technology,
 No. 1 University Rd., Yanchao District, Kaohsiung City 824, TAIWAN.
 *jcyu@nkust.edu.tw

Abstract: This paper presents a novel design of the 3-layer winding coil sets of a coreless axial-flux permanent-magnet generator applied to small wind turbines. The proposed generator design consists of two rotors and an integrated stator with flattened winding coil sets of three-phase three layers connected using a wye configuration. An analytical model of the inductance and resistance of the coil set is described to analyse the influence of the coil shape variation due to winding imperfection. The air gap magnetic flux distribution analysis shows the advantage of the integrated flatten coil sets compared with a typical stack up three layers stator. An experimental design is conducted for the parameter design of geometric variables to optimize the output power of the proposed AFPM design. A prototype generator is then constructed to compare with a benchmark generator that has a rated output power of 300 W at 800 rpm. The proposed design outperforms the benchmark generator by 26.5% in terms of generated power at a typical driving rotation velocity of 500 rpm for a small wind turbine, and demonstrates a superior performance at a lower driving speed range, which is particularly important in a small wind turbine application.

NOMENCLATURE

A_g	Effective cross-sectional area of each air gap	N_c	Number of coils per phase
A_r	Average flux passing areas of the rotor back iron behind PM regions	N_t	Number of turns per coil
A_{r1}	Average flux passing areas of the rotor back iron behind the inter polar	n	Rotor rotation speed
A_{r2}	Average flux passing areas of the rotor back iron behind PM regions	p	Number of poles
a	Number of parallel connected circuits	Q	Number of coil in one layer
B_g	Flux density in the airgap	q	Number of stator coils per phase
B_p	Peak value of the air-gap flux density	R_{aI}	Stator resistance of each phase of the winding Type I
C	Machine parameter	R_{aII}	Stator resistance of each phase of the winding Type II
E_l	Induced voltage	R_r	Reluctance of the rotor back iron
F_m	Magnetic field strength	R_{r1}	Reluctance behind the inter polar regions of back iron
g	Airgap between the rotor and stator	R_{r2}	Reluctance behind the magnet of back iron
h_a	Axial thickness of stator coil	R_m	Reluctance of the magnet in layer
k_{aI}	Distribution factor of Type I winding design	R_{mr}	Reluctance of the magnet to rotor back iron leakage flux
k_{aII}	Distribution factor of Type II winding design	R_{mm}	Reluctance of the magnet to magnet leakage flux
k_e	End-winding factor	R_g	Reluctance of the airgap
k_n	Nagaoka constant	r_b	Mean radius of stator winding, i.e., $(r_i + r_o)/2$
k_{pI}	Pitch factor of Type I winding design	r_i	Inner radius of magnet
k_{pII}	Pitch factor of Type II winding design	r_o	Outer radius of magnet
k_r	Radius factor	S_c	Area of one conductor cross section
k_w	Winding factor	S_p	Arc length of one coil pitch at the outer radius r_o of the magnet
L_I	Inductance of winding type I one layer	S_{pI}	Arc length of one coil pitch of the winding Type I at the outer radius r_o of the magnet
L_{II}	Inductance of winding type II one layer	S_{pII}	Arc length of one coil pitch of the winding Type II at the outer radius r_o of the magnet
L_{pm}	Magnetic thickness	T_{ac}	Motor torque output
L_{pm1}	Gap between two adjacent magnets	w_b	Width of coil band at the mid radius of the magnet
L_{pm2}	Arc length of the magnet at outer diameter	w_i	Width of coil band at the inner radius of the magnet
l_a	Coil length of the active conductor of stator winding	w_o	Width of coil band at the outer radius of the magnet
l_{eI}	Average total end-turn length of stator coil of the winding Type I	ω_e	Electrical rotating velocity
l_{eII}	Average total end-turn length of stator coil of the winding Type II	τ_p	Pole pitch length
l_g	Length of the airgap	θ_b	Radians of coil band at the mean radius r_b
m	Number of phase	θ_{mI}	Radians of coil band midline pitch of the winding Type I
		θ_{mII}	Radians of coil band midline pitch of the winding Type II
		θ_p	Radians of one coil pitch
		ρ_{cu}	Copper density of material

ϕ_m	Magnitude of magnet flux
ϕ_g	Magnitude of airgap flux
ϕ_{mr}	Magnitude of magnet to rotor back iron leakage flux
ϕ_{mm}	Magnitude of magnet to magnet leakage flux
ϕ_r	Magnitude of rotor back iron flux
μ_0	Absolute permeability, i.e., $4\pi \times 10^{-7}$ (H/m)
μ_r	Relative permeabilities of the rotor iron parts in the corresponding layer

1. Introduction

Radial generators have been widely used in automobiles, ships, wind-power, and other applications. However, radial generators often require high rotational speeds and large starting torque, and realizing the low cogging-torque characteristics for small wind-power generation is difficult, especially in low wind-speed regions. Axial ironless generators enjoy the advantage of low starting torque, which is suitable for low wind-speed applications. A considerable increase in the interest in permanent-magnet (PM) generators has arisen for applications in small wind turbines owing to their characteristics in terms of compactness, high efficiency, reliability, and self-excitation. Wind-power generation primarily converts wind energy into mechanical energy through the rotating blades of the wind turbine, using the converted mechanical energy to drive a generator to produce electrical energy. Axial-flux PM (AFPM) generators are well known to offer the advantages of high-aspect-ratio planar structures, compactness, relatively high torque density, and low cogging torque. Owing to their high torque capability, AFPM generators have become a feature in a direct-driven wind-energy conversion system at low wind-speed.

The earliest axial generators consisted of a single rotor and a single stator. However, a single-sided axial magnet generator will result in excessive axial attraction [1]. A double-sided permanent magnet rotor with a single stator [2][3] can offset the axial attraction and increase the output power at the cost of an increased weight. The double-sided permanent magnet rotor design can also reduce bearing wear and noise problem compared with a single-sided structure, which thus increases the generator reliability.

Concentrated windings are preferred for the applications of flat axial permanent magnet generators compared with distributed windings due to a shorter end turn length and a simpler structure [4], which increases the torque and winding factors. From a proper selection of pole-slot combinations, concentrated windings can provide a lower copper loss and a higher output power than normal overlapping winding [5].

Stator design of AFPM generators should consider core and windings. Stator cores can increase output power, but require a larger actuating torque to offset the axial attraction. The ironless design of an AFPM machine can reduce the attractive forces between the rotors and stators, which can alleviate the generator structural loads, and reduce any associated eddy-current and hysteresis core losses [6]. Therefore, the coreless design, is suitable for small wind turbine applications [7].

Conventional stator designs adopt a three phase single layer winding. Multiple layers of windings can reduce the space harmonics in the magnetomotive force of winding. The excitation of the coil is activated by the band on both sides by cutting the magnetic field of the magnet. Multiple layer windings have more band area ratio, and thus generate a higher output power. V. Rallabandi et al. [8] compares various designs of different number of layers and shifting angles, and suggests a four layer winding to minimize the cogging torque. However, due to the dimensional constraint of the annular sector coil of small wind turbines, the overlap of the bands of multiple layers increase significantly as the number of layers increases. The induced mutual inductance of overlapped bands will decrease the output power.

Three-layer concentrated winding [9][10] provides a higher coil factor, a higher number of coils, smaller eddy current losses, and smaller torque ripple. But three-layer winding is liable to the electromotive force (EMF) imbalance. According to the air gap flux

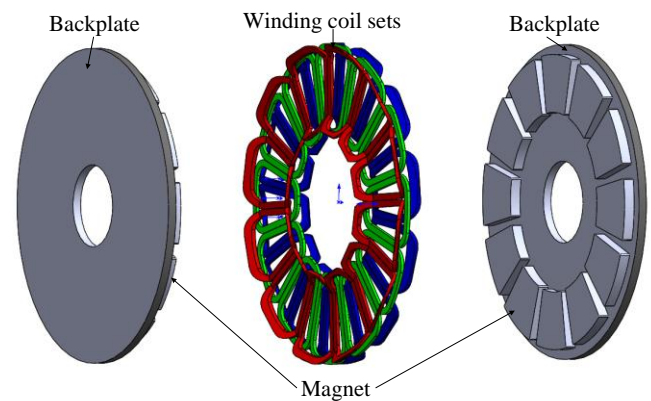


Fig. 1 Schematic assembly of the proposed AFPM generator consisting of two rotors and one integrated stator

distribution analysis [11], the outer layers of the winding are closer to the rotor magnet, and thus have higher magnetic flux densities compared with the middle layer. Therefore, the ratio of the back EMF of the middle layer is smaller than the other two, which eventually leads to large torque fluctuations and vibrations. If the overlap coils can be bent with all the active conductors lying in one plane, the air gaps of all three phases will be evened out [12]. Moreover, the structure of such machines makes them sensitive to geometrical imperfections [13] due to winding process. The variations of the air gap flux density due to the offset and the tilt of rotor disks result in unbalanced magnetic forces and torques.

Due to the elimination of the magnetic core on the stator, the coil design is more flexible but sensitive to the number of rotor poles for ironless stator AFPM machines. The slot-pole combination is a vital aspect of optimization for the improvement of torque and power density. Wang et al. [14] investigated the influence of slot-pole combination on the comprehensive performance of the ironless stator AFPM machine with non-overlapping concentrated windings. Khan et al. [15] proposed a two-stack coreless AFPM machine with a coreless inner-rotor structure for low-speed applications to reduce core losses and improve output efficiency. Some suggested a compound structure machine which connects an axial magnetic-field-modulated brushless double-rotor machine (AMFM-BDRM) with a traditional permanent-magnet synchronous machine for the applications of series-parallel hybrid electric vehicles [16]. The double-sided AMFM-BDRM is recommended to eliminate the axial tilting torque compared with the single sided topology.

This paper presents a novel winding design of the coreless stator of an AFPM generator for small wind turbine generators. A dual-rotor single-stator with 3 layer concentrated winding AFPM generator is considered. Each layer of coils is one phase. To even the air gaps between three layers and dual-rotor magnets, a flattened bending technique is applied to embed and level the bands of three layers. Taguchi method is introduced for the parameter design of the equivalent magnetic circuit of the AFPM generator to increase the output power. Finally, a simplified 3D electromagnetic models are simulated using the finite-element analysis (FEA) to validate the superiority of the winding design. A prototype AFPM generator is constructed to compare the performance with a benchmark generator.

2. Design of the AFPM generator

Figure 1 shows that the proposed AFPM generator features the configuration of two identical rotor disks and an integrated ironless stator disk. Two rotor disks consisting of 12 poles of NdFeB rare-earth PMs and a backplate are directly connected to the input shaft. The integrated stator-coil disk consists of three layers of sinusoidal windings designated as U, V, and W, which are connected using a wye configuration. Each phase of the concentrated winding coil has 12 coils. The coils in each phase are arranged with a phase difference of 10 degree to allow for uniform cutting of the flux fields. The designed three-layer winding is shown in Fig. 2.

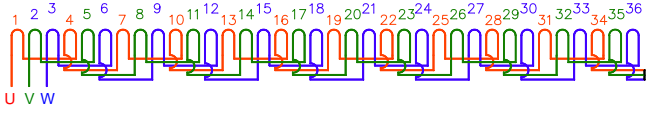


Fig. 2 Wiring mode of the winding coil set

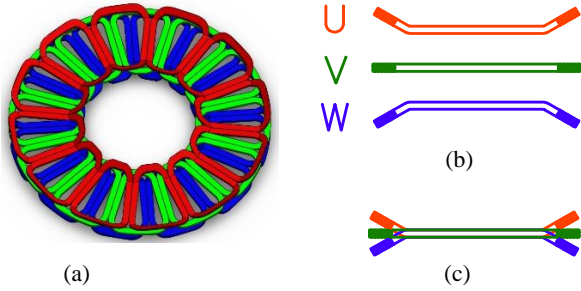


Fig. 3 Schematic drawing of the integrated stator-coil disk (a) Assembly of U, V, W winding coils, (b) three phase coils, (c) Assembly of flattened U, V, W coils

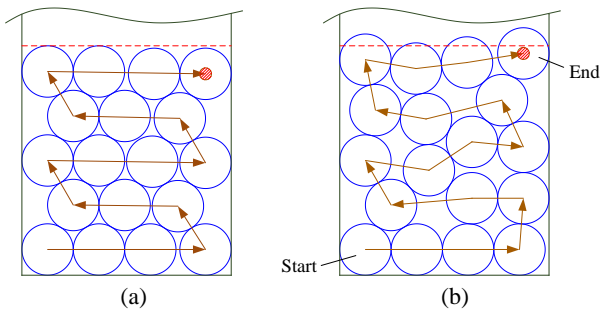


Fig. 4 Coil winding: (a) left side without overline condition and (b) right-side cross-line condition

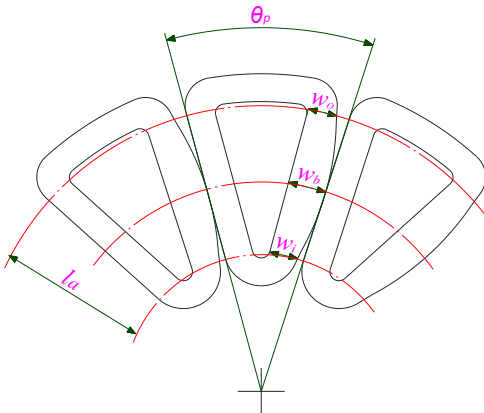


Fig. 5 Schematic layout of the air-coil concentrated winding stator with shape deformation

Figure 3 shows a schematic layout of the flattened U, V, and W winding coil sets. The three layers of winding coil sets are coreless to reduce the cogging-torque effect and core losses, and molded with resin to improve mechanical strength. Typical three-layer winding coil sets apply a simple stack up layout, which is liable to the electromotive force (EMF) imbalance due to the difference of the air gaps in the middle layer and the outer layers. The stator-coil disk in this study adopts a flattened integrated design by first bending U and W winding coil sets before stacking up with the V coil set as in Fig.3(b). Therefore, all the active conductors lie in one plane, which keeps the distances between the coil set and the rotor magnets the same for all three phases to reduce cogging problems.

3. Modelling of the coil winding

3.1. Shape Imperfection of the Coil Winding

Ideally, the coil winding should have a coil pitch of 180 electrical degrees. However, during wire winding in the cavity, the coil winding tends to bulge at the side with the overlap region at the end of one layer and the start of the next layer because the wire is not stacked in the cavity between the lines of the last layer, as shown in Fig. 4(b). The bulge in the coil shape will result in a coil pitch of less than 180 electrical degrees, as shown in Fig. 5. The influence of manufacturing errors is analysed using a simplified model in the following discussion.

3.2. Theoretical Characteristics of Ideal Concentrated Coil Winding

Fig. 6 shows the Type I winding that we use to illustrate the case of ideal winding as well as to analyse the torque, inductance, and resistance of the generator. The magnet is installed above the coil. Induced voltage EI of the Type I winding is expressed in (1) [17].

$$E_I = \frac{q}{a} \frac{4}{p} \omega_e B_p N_t r_b l_a k_{pl} k_{dl} \quad (1)$$

$$B_p = \frac{2\sqrt{3}B_g}{\pi} \quad (2)$$

$$k_{pl} = \sin\left(\frac{S_{pl} - W_b}{\tau_p} \frac{\pi}{2}\right) \quad (3)$$

$$k_{dl} = \frac{\sin\left(\frac{n(\theta_{ml} - \pi)}{2}\right)}{\sin\left(\frac{\theta_{ml} - \pi}{2}\right)} \quad (4)$$

Fig. 6 shows that for $0 \leq \Delta\theta \leq \theta_b$, torque output T_{ac} can be determined as follows:

$$T_{ac} = k_w k_e k_r C \quad (5)$$

$$k_w = k_{pl} k_{dl} \sqrt{\theta_b \frac{q}{p}} \quad (6)$$

$$\theta_b = \left(\frac{r_i - l_g}{r_b}\right) \frac{\pi}{3} \quad (7)$$

$$k_e = \left(2 + \frac{l_{el}}{l_a}\right)^{-\frac{1}{2}} \quad (8)$$

$$k_r = \sqrt{\left(1 + \frac{r_i}{r_0}\right)^3 \left(1 - \frac{r_i}{r_0}\right)} \quad (9)$$

The inductance of the phase winding consists of the mutual and leakage inductances. The proposed AFPM adopts a coreless stator winding with a smaller inductance than the stator winding with an iron core. Inductance LI of the winding can be calculated as follows:

$$L_I = \frac{q(2l_a + l_{el})^2 N_t^2}{h_a} 10^{-7} k_n \quad (10)$$

The phase resistance of the stator winding leads to a copper loss in the AFPM generator. Stator resistance R_{al} in each phase in the Type I winding can be obtained as follows:

$$R_{al} = \rho_{cu} \left(2l_a + \frac{4\pi R_e}{Q}\right) \frac{N_c Q}{3S_c} \quad (11)$$

3.3. Theoretical Characteristics of Imperfect Concentrated Coil Winding

Fig. 5 shows that the band width w_b in the mid-section of the bulged winding will be larger than the band width w_o in the outer section, which causes a gap between two adjacent coils. However, an

analysis of the exact winding characteristics is very complicated. A Type II winding as shown in Fig. 7 is applied in this study to analyse the effects of the winding with shape imperfection. Ideally, the pitch of the coil band midline of the winding, θ_{ml} is the same as the coil pitch θ_p in Fig. 6. To simulate the effects of bulged winding, the shape of the air-coil remains a sector in Type-II winding, but the occupied pitch of the coil band midline, θ_{mII} is smaller than the ideal coil pitch θ_p , which results in a gap at the top of coil assembly as shown in Fig. 7. The corresponding dimensions of Types I and II windings are listed in Table 1.

In the Type II winding, only the inner radii of the coil touch one another. Therefore, the pitch factor [10] is given by

$$k_{pII} = \sin\left(\frac{S_{pII} - W_b}{\tau_p} \frac{\pi}{2}\right) \quad (12)$$

The distribution factor of the Type II winding becomes

$$k_{dII} = \frac{\sin\left(\frac{q(\theta_{mII} - \pi)}{2}\right)}{\sin\left(\frac{\theta_{mII} - \pi}{2}\right)} \quad (13)$$

The inductance of the Type II winding becomes

$$L_{II} = \frac{\sqrt{3}[q(2l_a + l_{el})^2 N_f^2]}{2h_a} 10^{-7} k_n \quad (14)$$

Stator resistance R_{all} in each phase can be obtained as follows:

$$R_{all} = \rho_{cu} \left(2l_a + \frac{2\theta_{mII} R_e}{p}\right) \frac{N_c Q}{3S_c} \quad (15)$$

Equations (10) and (14) demonstrate that the inductance of the Type II winding is smaller than that of the Type I winding. Obviously, the magnetic field density of the Type II winding is lower than that of the Type I winding.

3.4. Influence of Winding Imperfection

The design of the Type I winding features a uniform coil band width, and each band is snugly adjacent to the neighboring band in the next coil. When the coil is excited, the magnet rotates to smoothly cut the magnetic field without any cogging problem. However, the Type II winding shows a gap between the neighboring bands of the adjacent coils to simulate the effect due to bulged winding as shown in Fig. 5. The magnetic field density in the gap is very low, resulting in a cogging problem when the magnet rotates to cut the magnetic field, which leads to a decrease in the power generation.

The two generators based on the above mentioned winding designs are fabricated to analyse the influence of winding imperfection on the generator performance. A 10- Ω resistor is used as a charging load of the generator. The generator parameters are listed in Table 2. Fig. 8 shows the comparison of the generated current of the Type I and Type II windings. The generated currents increase in linear proportion to the driving speed, and gradually saturate for the speeds higher than 600 rpm due to a temperature rise leading to an increase of copper loss. The winding imperfection in the Type II winding results in about 15% power loss at the speed of 600 rpm compared with the ideal winding in Type I. The gap among coils at the top of coil assembly in Fig. 7 will not only reduce the generated power, but also cause a cogging problem liable for mechanical vibrations. Therefore, the reduction in shape imperfection of coil during the winding process is important to increase the power efficiency.

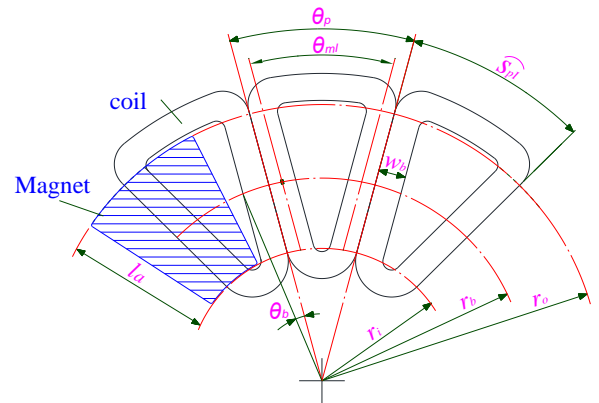


Fig. 6 Layout of the air-coil concentrated Type I winding stator

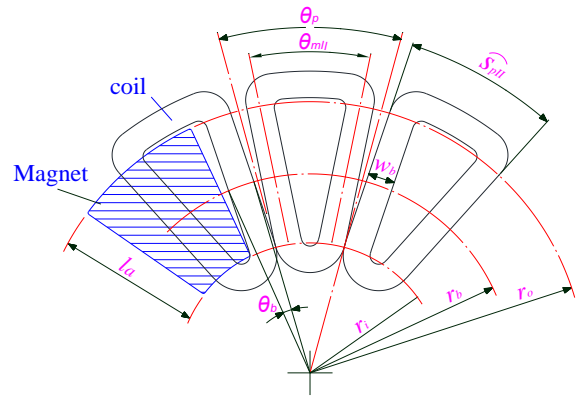


Fig. 7 Simplified model of the Type II winding with shape imperfection

Table 1 Dimensions of Types I and II winding coils

	Type I	Type II
θ_p	30°	30°
θ_m	30°	23°
θ_b	7.6°	7.6°
S_p (mm)	38.8	33.8
l_a (mm)	34.5	34.5
w_b (mm)	6.5	6.5
w_o (mm)	6.5	6.5
w_i (mm)	6.5	6.5
r_b (mm)	32.1	32.1
r_i (mm)	66.6	66.6
r_o (mm)	48.8	48.8

Table 2 AFPM generator parameters

Number of phases, m	3
Number of stator slots, q	12
Winding type	Three-layer coil sets
Number of rotor poles, p	12
Air gap, g (mm)	1.0
Outer stator diameter, r_o (mm)	150
Inner stator diameter, r_i (mm)	36
Magnetic thickness, L_{pm} (mm)	5
Magnetic length, l_a (mm)	40
Magnetic material	NdFeB,N38SH

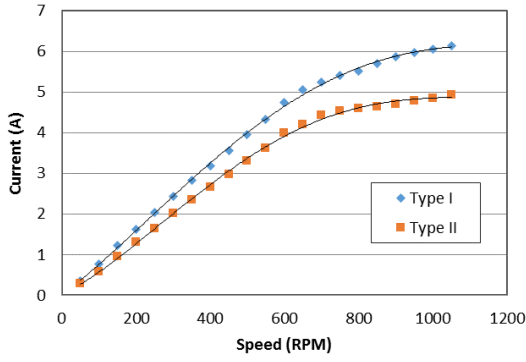


Fig. 8 Comparison of the generated current vs. speed for the Type I and Type II windings

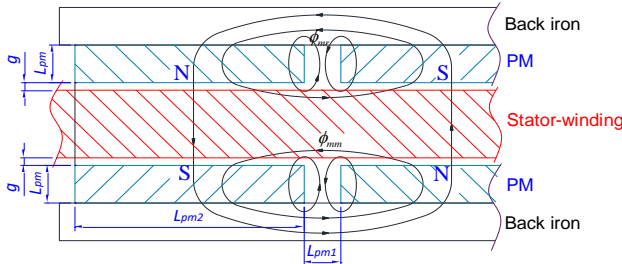


Fig. 9 2D structure diagram of a ironless AFPM design

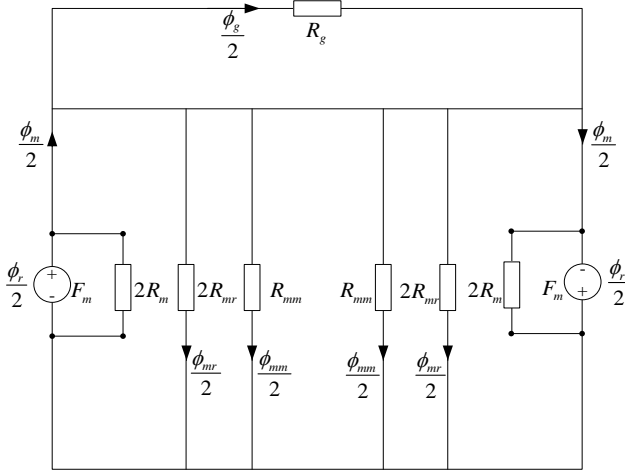


Fig. 10 Equivalent magnetic circuit model of the AFPM design in Fig. 9

4. Modelling of the AFPM generator

4.1. Magnetic Equivalent Circuit Model

In this paper, a 2D model of the magnetic-flux path is shown in Fig. 9 [18]. Its equivalent magnetic circuit model is shown in Fig. 10.

To consider the reluctance of the rotor back iron and the magnetic field density, the equations of the corresponding reluctances shown in Fig. 10 are expressed as follows:

$$R_{r1} = \frac{L_{pm1}}{\mu_0 \mu_r A_{r1}} \quad (16)$$

$$R_{r2} = \frac{0.5L_{pm2}}{\mu_0 \mu_r (A_{r1} + A_{r2}) / 2} \quad (17)$$

$$R_r = R_{r1} + 2R_{r2} \quad (18)$$

$$R_m = \frac{L_{pm}}{\mu_0 \mu_r L_{pm2} (r_{mo} - r_{mi})} \quad (19)$$

$$R_{mr} = \frac{L_{pm1}}{\mu_0 \mu_r L_{pm} (r_{mo} - r_{mi})} \quad (20)$$

$$R_{mm} = \frac{\pi}{\mu_0 (r_{mo} - r_{mi}) \ln(1 + \frac{\pi g}{L_{pm1}})} \quad (21)$$

$$R_g = \frac{g}{\mu_0 A_g} \quad (22)$$

$$A_g = \frac{\pi L_{pm2} ((2r_{mo} + g)^2 - (2r_{mi} - g)^2)}{12p} \quad (23)$$

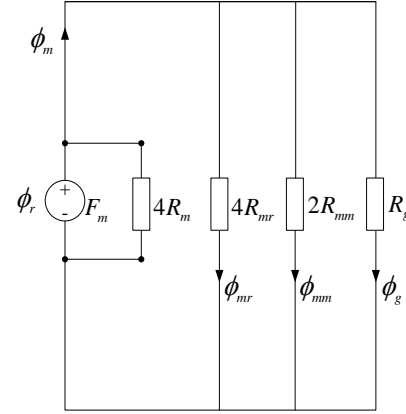


Fig. 11 Simplified equivalent magnetic circuit model of an AFPM generator

Considering the symmetry of the magnetic circuit, Fig. 10 can be simplified into Fig. 11 where each airgap main flux is expressed as ϕ_g in (24). Total magnetic-flux ϕ_m in (25) is generated by the outward magnetic path of each pole magnet. The magnet-to-magnet leakage flux is expressed as ϕ_{mm} in (26), the leakage flux of the rotor back iron to the magnet is defined as ϕ_{mr} in (27), and the rotor back iron and magnets generate magnetic-flux ϕ_r .

$$\phi_g = \frac{\phi_r}{1 + \frac{R_g}{R_m} (1 + \frac{R_m}{R_{mr}} + 2(\frac{R_m}{R_{mm}}))} \quad (24)$$

$$\phi_m = \phi_r \frac{1 + \frac{R_g}{R_m} (\frac{R_m}{R_{mr}} + 2(\frac{R_m}{R_{mm}}))}{1 + \frac{R_g}{R_m} (1 + \frac{R_m}{R_{mr}} + 2(\frac{R_m}{R_{mm}}))} \quad (25)$$

$$\phi_{mm} = \phi_r \frac{1 + \frac{R_g}{R_m} (\frac{R_m}{R_{mr}})}{1 + \frac{R_g}{R_m} (1 + \frac{R_m}{R_{mr}} + 2(\frac{R_m}{R_{mm}}))} \quad (26)$$

$$\phi_{mr} = \phi_r \frac{1 + \frac{R_g}{R_m}}{1 + \frac{R_g}{R_m} (1 + \frac{R_m}{R_{mr}} + 2(\frac{R_m}{R_{mm}}))} \quad (27)$$

According to (24)–(27), we obtain

$$\begin{bmatrix} \phi_m \\ \phi_g \\ \phi_{mr} \\ \phi_{mm} \\ \phi_r \end{bmatrix} = \begin{bmatrix} 4R_m & 0 & 4R_{mr} & 0 & 0 \\ 0 & R_g & 0 & -2R_{mm} & 0 \\ 0 & 0 & -4R_{mr} & 2R_{mm} & R_r \\ -0.5 & 0.5 & 1 & 1 & 0 \\ 0.5 & 0 & -1 & 0 & -1 \end{bmatrix}^{-1} \begin{bmatrix} F_m \\ 0 \\ 0 \\ 0 \\ 0 \end{bmatrix} \quad (28)$$

$$F_m = \phi_m R_m = \frac{1 + \frac{R_g}{R_m} \left(\frac{R_m}{R_{mr}} + 2 \left(\frac{R_m}{R_{mm}} \right) \right) L_{pm}}{1 + \frac{R_g}{R_m} \left(1 + \frac{R_m}{R_{mr}} + 2 \left(\frac{R_m}{R_{mm}} \right) \right) \mu_0 \mu_r L_{pm} 2 (r_{mo} - r_{mi})} \phi_r \quad (29)$$

The equivalent magnetic circuit model in Fig. 11 shows that magnetic field strength F_m is enhanced with the increase in R_m .

4.2. Simulation of the AFPM Generator

Here, the study applies FEA to compare the induced voltages of a typical stack up three layers of winding coil sets and the proposed flattened integrated design. Typical stack up winding coil sets adopt one phase in each layer as shown in Fig. 12(a). The air gaps of all three winding coil sets are different, which results in a larger variation of the magnetic-flux density among three coil sets as shown in Fig. 12(b). The induced voltage in the middle coil set is 15% lower than those in the other two phases, as shown in Fig. 13(a), because of a lower electromotive force, which leads to a cogging problem and mechanical vibrations.

Figure 14(a) shows the schematic structure of the flattened integrated stator-coil disk. Since all the active conductors of the flattened winding coil sets lie in one plane, the air gaps of all three phases are the same. The simulation in Fig. 14(b) demonstrates that the magnetic-flux densities of all three phases are much more even compared with the distribution of the typical stack up winding coil sets in Fig. 12(b), which leads to a uniform induced voltages of all three phases as shown in Fig. 13(b). The induced peak voltage of the proposed design is 20% higher than the voltage of a typical stack up design.

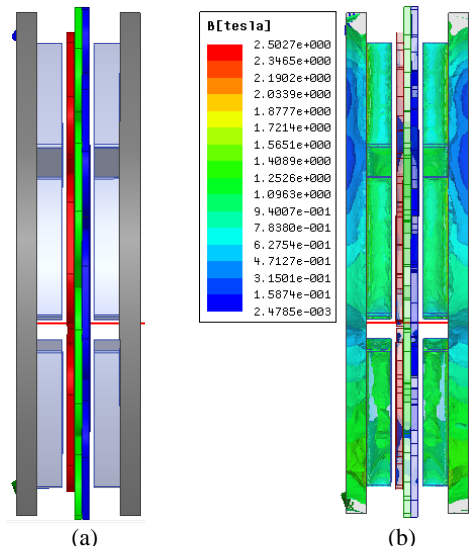


Fig. 12 FEA simulation of the magnetic-flux distribution for typical stack up winding coil sets of three layers. (a) Schematic structure, (b) Distribution of magnetic-flux density

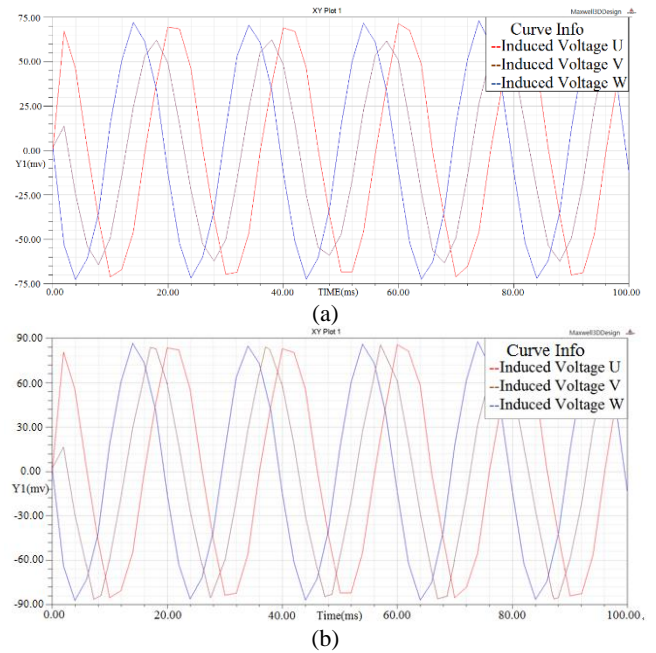


Fig. 13. Induced voltages in the three phases for (a) typical stack up winding coil sets and, (b) flattened winding coil sets

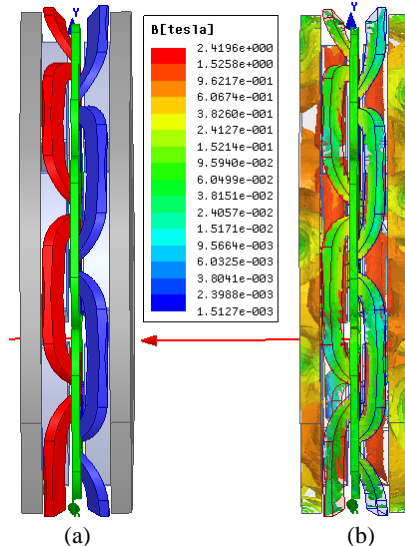


Fig. 14 FEA simulation of the magnetic-flux distribution for the flattened winding coil sets. (a) Schematic structure, (b) Distribution of magnetic-flux density

5. Parameter optimization using experimental design

An experimental design is used to optimize the parameter design of the proposed AFPM. The design factors include the wire diameter, number of turns, number of poles, and air gap. Each factor consists of three levels, as listed in Table 3. The orthogonal array of L18 is used as the experimental design for parameter optimization. Eighteen test generators are fabricated according to the parameter designs of L18 to measure the corresponding output power. Fig. 15 shows a prototype of the test AFPM generator. Fig. 15(a) shows the sample coil wound using enameled wire. Each phase of the concentrated winding coil consists of 12 coils, and three layers of winding coil sets are packaged to an integrated stator, as shown in Fig. 15(b). The total weight of the winding coil sets is approximately 224 (g). The stator is assembled with two rotors as shown in Fig. 15(c) to function as the test generator, as shown in Fig. 15(d).

The design objective is to maximize the output power of the AFPM. A generator-testing platform is constructed to investigate the operating performance of the test generator, as shown in Fig. 16. The

drive motor of the generator is a PM synchronous motor. The driving speed of the motor is given as 500 rpm, while the driving torque is measured using a torque meter to calculate the input wind energy. A 10-Ω resistor is applied as a load. The output power of the generator is measured as the performance index. The output power values of the sample generators using L18 are listed in Table 4.

Table 3 Factorial design of the parameters

Factor level	A Wire diameter (mm)	B Number of turns in coil	C Number of poles	D Air gap (mm)
Level 1	Φ 0.37	30	10	1
Level 2	Φ 0.40	33	12	2
Level 3	Φ 0.45	36	16	3

The effect plot that employs analysis of the mean is shown in Fig. 17. To verify the effectiveness of the experimental design, the result of the analysis of variance (ANOVA) of the design variables is listed in Table 5. All factors are significant with significance level of 0.01. Because the design objective is to maximize the output power of the generator, the optimum parameter design is A3B2C2D1, which corresponds to a wire diameter of 0.45 mm, 33 turns of coil, 12 poles, and the air gap of 1.0 mm. The optimally designed generator is fabricated, and the corresponding output power using the test platform is 152 W. The optimal design is superior to the best design in L18, which is No. 7, with output power of 146.2 W.

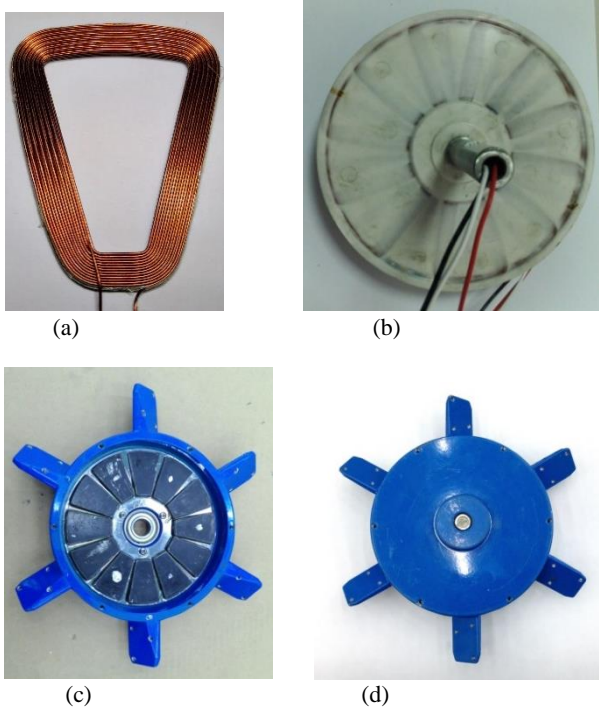


Fig. 15 Prototype AFPM generator: (a) coil, (b) molded stator, (c) rotor, and (d) generator assembly

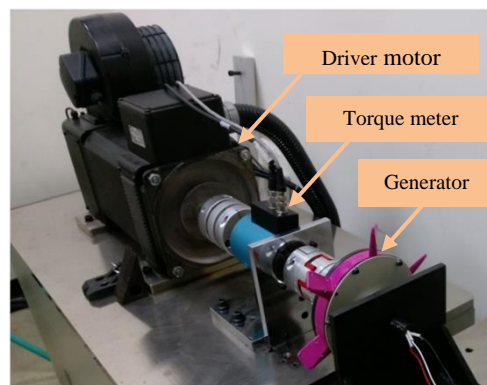


Fig. 16 Test platform of the generator

Table 4 Design of experiments using L18

EXP.	A	B	C	D	Input Torque (Nm)	Output power (Watt)
1	1	1	1	1	6.39	135.8
2	1	2	2	2	6.43	138.8
3	1	3	3	3	6.23	124.6
4	2	1	1	2	6.24	128.0
5	2	2	2	3	6.46	140.8
6	2	3	3	1	6.41	136.8
7	3	1	2	1	6.54	146.2
8	3	2	3	2	6.48	141.8
9	3	3	1	3	6.33	134.4
10	1	1	3	3	6.22	126.4
11	1	2	1	1	6.42	137.8
12	1	3	2	2	6.32	133.6
13	2	1	2	3	6.30	131.2
14	2	2	3	1	6.46	140.8
15	2	3	1	2	6.30	129.8
16	3	1	3	2	6.41	136.8
17	3	2	1	3	6.48	141.8
18	3	3	2	1	6.51	145.4

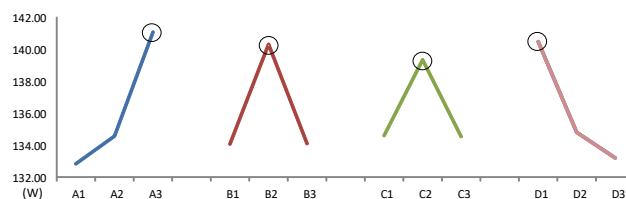


Fig. 17 Effect plot of the design factors

6. Comparison of designs

The proposed generator design is compared with a benchmark generator from the market. The parameters of the benchmark generator with a rated output power of 300 W at 800 rpm are listed in Table 6. The rotor disks consist of 12 poles of NdFeB rare-earth PMs supported by two backplates. The winding system of the stator adopts typical two-layer coil sets where the U, V, and W coils are interlaced and overlapped between the two coil sets. To better understand the performance in the application to a small wind turbine, the output power of both generators are measured using a power analyzer, YOKOGAWA WT1806E, at the driving speeds from 50 to 1000 rpm, as shown in Fig. 18; the corresponding driving torque and current are shown in Fig. 19. The output power of the proposed design is better than that of the benchmark generator within the test-speed range. The typical driving speed of a small wind turbine is assumed below 500 rpm. The power of the proposed

design is 162 W which is 26.5% higher than the 128 W of the benchmark generator with a slight increase of 15.3% in the driving torque at the speed of 500 rpm. The comparison of the efficiency in Fig. 20 also shows the superiority of the proposed design in a low-speed application. The efficiency of the proposed design is about 25% better than the benchmark generator at a driving speed lower than 100 rpm.

Table 5 ANOVA of the output power

Design Parameters	SS	DOF	MS	F
A	226.08	2	113.04	37.51
B	154.59	2	77.30	25.65
C	90.90	2	45.45	15.08
D	174.95	2	87.48	29.03
Error	27.1	9	3.0	
Total Sum of Squares	673.64	17		

Table 6 Winding parameters and dimensions of the studied generators

	Proposed Design	Benchmark Generator
Number of phases, m	3	3
Number of stator slots, q	12	9
Winding type	Three-layer coil sets	Two-layer coil sets
Number of rotor poles, p	12	12
Outer stator diameter, r_o (mm)	150	160
Inner stator diameter, r_i (mm)	36	36
Magnetic thickness, L_{pm} (mm)	5	5
Magnetic length, l_a (mm)	40	42

7. Conclusion

This paper has presented a novel design of the 3-layer winding coil sets of stator of a coreless axial-flux permanent-magnet generator for small wind turbines. The three-layer coil sets with wye configuration are integrated into the stator. Each layer of concentrated winding coil with 12 coils corresponds to a phase. The coils in each phase are arranged with a phase difference of 10 degrees to produce uniform cutting of the flux fields. An analytical model of the inductance and resistance of the stator is presented to analyse the influence of the coil geometry variation due to winding imperfection. The proposed coreless stator design with flattened winding coil sets greatly improves the fluctuations of induced voltage and increases the output power. The comparison between the proposed design and a benchmark generator using the test platform demonstrates that the proposed design outperforms the benchmark generator in terms of the generated power and the efficiency for the driving speeds lower than 500 rpm, which is particularly important for the applications of small wind turbines.

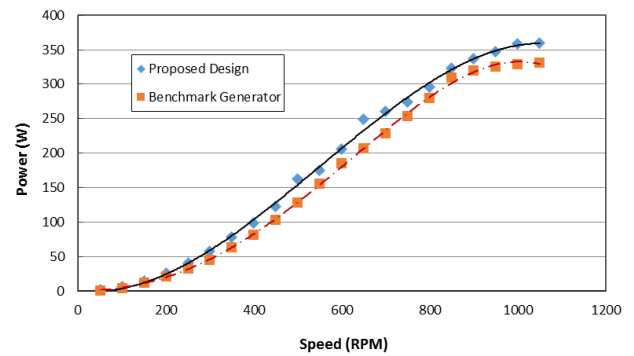


Fig. 18 Comparison of the output power between the proposed design and the benchmark generator

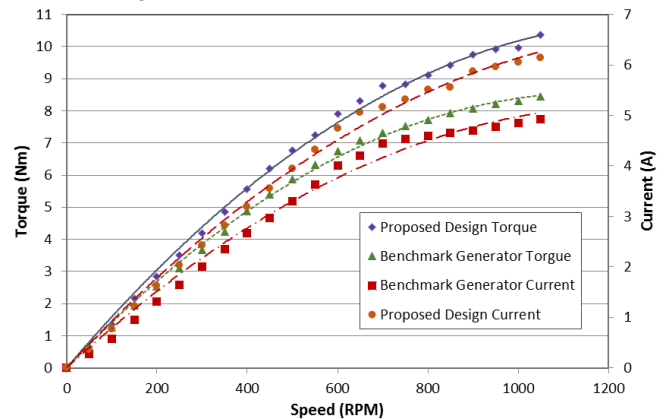


Fig. 19 Comparison of the torque and current between the proposed design and the benchmark generator

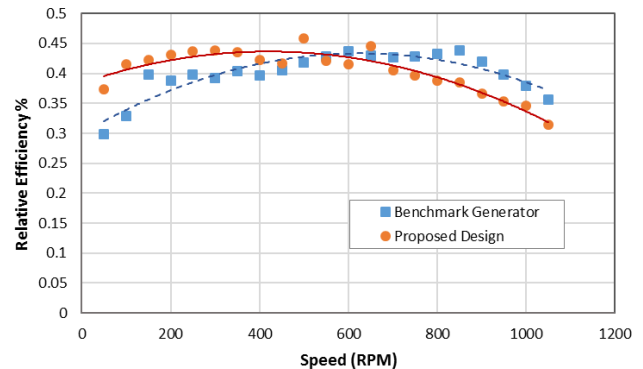


Fig. 20 Comparison of the efficiency between the proposed design and the benchmark generator

8. References

- [1] C.-T. Liu, T.-S. Chiang, J. F. Diaz Zamora and S.-C. Lin, "Field-oriented control evaluations of a single-sided permanent magnet axial-flux motor for an electric vehicle," *IEEE Trans. On Magnetics*, 2003, 39, (5), pp. 3280-3282.
- [2] S.Y. Sung, J.H. Jeong, Y.S. Park, J. Y. Choi and S. M. Jang, "Improved Analytical Modeling of Axial Flux Machine With a Double-Sided Permanent Magnet Rotor and Slotless Stator Based on an Analytical Method," *IEEE Trans. on Magnetics*, 2012, 48, (11), pp. 2945-2948.
- [3] F. G. Gaponi, G. D. Donato, G. Borocci and F. C. Caricchi, "Axial-Flux Hybrid-Excitation Synchronous Machine: Analysis, Design, and Experimental Evaluation," *IEEE Trans. on Industry Application*, 2014, 50, (5), pp. 3173-3184.
- [4] H. Vansompel, P. Sergeant, L. Dupre and A. Bossche, "A Combined Wye-Delta Connection to Increase the Performance of Axial-Flux PM machine with Concentrated Windings," *IEEE Trans. on Energy Conversion*, 2012, 27, (2), pp. 403-410.
- [5] M.J. Kamper, R.J. Wang and F.G. Rossouw, "Analysis and Performance of Axial Flux Permanent-Magnet Machine With Air-Cored Nonoverlapping Concentrated Stator Windings," *IEEE Trans. on Industry Applications*, 2008, 44, (5), pp. 1495-1504.

- [6] A. A. Arkadan, T.M. Hijazi and B. Masri, "Design Evaluation of Conventional and Toothless Stator Wind Power Axial-Flux PM Generator," *IEEE Trans. on Industrial Applications*, 2017, 53, (6), 8104404.
- [7] E. Spooner, P. Gordon, J.R. Bumby and C.D. French, "Lightweight ironless-stator PM generators for direct-drive wind turbines," *IEE Proceedings - Electric Power Applications*, 2005, 152, (1), pp. 17-26.
- [8] V. Rallabandi, N. Taran and D.M. Ionel, "Multilayer Concentrated Windings for Axial Flux PM Machines," *IEEE Trans. on Magnetics*, 2017, 53, (6), 8103104.
- [9] T. Cox and J. F. Eastham, "Multi-layer planar concentrated Windings," 2011 IEEE International Electric Machines & Drives Conference (IEMDC), Niagara Falls, ON, 2011, pp. 1439-1444.
- [10] B. Xia, J.X. Shen, C.K. Luk and W. Fei, "Comparative Study of Air-Cored Axial-Flux Permanent-Magnet Machines With Different Stator Winding Configurations," *IEEE Trans. on Industrial Electronics*, 2015, 62, (2), pp. 846-856.
- [11] Y. Huang, B. Ge, J. Dong, H. Lin, J. Zhu and Y. Guo, "3-D Analytical Modeling of No-Load Magnetic Field of Ironless Axial Flux Permanent Magnet Machine," in *IEEE Transactions on Magnetics*, 2012, 48, (11), pp. 2929-2932.
- [12] Z. Zhang, A. Matveev, R. Nilssen and A. Nysveen, "Ironless Permanent-Magnet Generators for offshore Wind Turbines," *IEEE Trans. on Industrial Applications*, 2014, 50, (3), pp. 1835-1846.
- [13] A.D. Gerlando, G. M. Foglia, M. F. Iacchetti and R. Perini, "Effects of Manufacturing Imperfections in Concentrated Coil Axial Flux PM Machines: Evaluation and Tests," *IEEE Trans. on Industry Electronics*, 2014, 61, (9), pp. 5012-5024.
- [14] C. Wang, Z. Zhang, Y. Liu, w. Geng and H. Gao, "Effect of Slot-Pole Combination on the Electromagnetic Performance of Ironless Stator AFPM Machine with Concentrated windings," *IEEE Trans. On Energy Conversion*, 2020, 35, (2), pp. 1098-1109.
- [15] S. Khan, S. S. H. Bukhari and J. S. Ro, "Design and Analysis of a 4-KW Two Stack Coreless Axial Flux Permanent Magnet Synchronous Machine for Low Speed Applications," *IEEE Access*, 2019, 7, pp. 173748-173854.
- [16] M. Wang, C. Tong, Z. Song, J. Liu and P. Zheng, "Performance Analysis of an Axial Magnetic-Field-Modulated Brushless Double-Rotor Machine for Hybrid Electric Vehicles," *IEEE Trans. On Industrial Electronics*, 2019, 66, (1), pp. 806-817.
- [17] I. Stamenkovic, N. Milivojevic, N. Schofield and M. Krishnamurthy, "Design, Analysis, and Optimization of Ironless Stator Permanent Magnet Machines," *IEEE Trans. on Power Electronics*, 2013, 28, (5), pp. 2527-2538.
- [18] A. Daghigh, H. Javadi and H. Torkaman, "Design Optimization of Direct-Coupled Ironless Axial Flux Permanent Magnet Synchronous Wind Generator with Low Cost and High Annual Energy Yield," *IEEE Trans. on Magnetics*, 2016, 52, (9), 7403611.